CHEMISTRY
A European Journal

A Journal of
ChemPubSoc Europe

Accepted Article

Title: CoSe2/MoSe2 Heterostructures with Enriched Water Adsorption/ Dissociation Sites towards Enhanced Alkaline Hydrogen Evolution Reaction

Authors: Guoqiang Zhao, Peng Li, Kun Rui, Yaping Chen, Shi Xue Dou, and Wenping Sun

To be cited as: *Chem. Eur. J.* 10.1002/chem.201801693

Link to VoR: http://dx.doi.org/10.1002/chem.201801693

Supported by
ACES

WILEY-VCH

10.1002/chem.201801693

WILEY-VCH

$CoSe_2/MoSe_2$ Heterostructures with Enriched Water Adsorption/Dissociation Sites towards Enhanced Alkaline Hydrogen Evolution Reaction

Guoqiang Zhao,[a] Peng Li,[a] Kun Rui,[a] Yaping Chen,[a] Shi Xue Dou,[a] Wenping Sun[a,*]

Abstract: Transition metal dichalcogenides (TMDs) are promising electrocatalysts toward hydrogen evolution reaction (HER) in acid media, but they show significantly inferior activity in alkaline media due to the extremely sluggish water dissociation kinetics. Herein, $CoSe_2/MoSe_2$ heterostructures with $CoSe_2$ quantum dots anchored on $MoSe_2$ nanosheets are synthesized towards enhanced alkaline HER catalytic activity. The incorporation of $CoSe_2$ is intended to construct additional water adsorption sites on the basal planes of $MoSe_2$ to promote water dissociation. The $CoSe_2/MoSe_2$ heterostructures show substantially enhanced activity over $MoSe_2$ and $CoSe_2$ in 1 M KOH. The optimal overpotential required to reach a current density of 10 mA cm^{-2} is merely 218 mV, more than 100 mV superior than $MoSe_2$, which is by far the best performance demonstrated for precious metal-free catalysts. Detailed analyses based on the electrochemical testing demonstrate that the water adsorption and subsequent dissociation process is accelerated by the $CoSe_2$ species with rich edge sites; meanwhile, $MoSe_2$ species provide sufficient active sites for the adsorption and combination of the generated H^*. Our results provide an effective strategy for developing earth-abundant catalysts with high activity for alkaline HER, and are of great significance to promote the practical application of alkaline water electrolysis.

Introduction

The exploration and utilization of hydrogen gas (H_2) have drawn extensive attention in recent years because H_2, with the highest gravimetric energy density of all chemical fuels (142MJ kg^{-1}), is believed to be one of the most promising future energy carriers in view of environment protection and energy storage.[1] In particular, the underutilized renewable energy (e.g., solar energy, wind energy) could be efficiently converted into higher valuable H_2 by electrochemical water splitting (water electrolysis) with the help of appropriate catalysts,[2] which also ensures the widespread use of the renewable energy. However, the most efficient catalysts for water splitting at present are still precious metal-based materials, such as Pt, Pd, Ir, and Ru, and their large-scale application is seriously hindered by elemental scarcity and unaffordable high cost.[3] To date, it is still a great challenge to develop low-cost, stable, and effective catalysts for electrochemical water splitting. Tremendous progress has been made in developing cost-effective and earth-abundant catalysts with appealing catalytic performance in the past several years, especially for hydrogen evolution reaction (HER), the cathodic part of the overall water splitting process.[4] Transition metal dichalcogenides (TMDs),[5] transition metal phosphides and carbides,[6] and carbonaceous materials have recently been extensively studied as HER catalyst alternatives,[7] and several materials showed very impressive catalytic activity.[8]

As a typical type of TMDs, two-dimensional (2D) MoS_2 has been extensively investigated as an efficient HER catalyst due to the moderate adsorption energy of hydrogen on MoS_2 edges.[9] $MoSe_2$, an analogue of MoS_2, shows even better HER performance than MoS_2 because of its higher electric conductivity as well as moderate adsorption energy of hydrogen.[10] To make full use of the catalytic potential of these 2D TMDs, various modification approaches have been developed, including nanostructure designing,[11] heteroatom doping,[12] and defect engineering.[13] Constructing well-defined heterostructures is turned out to be an effective nanostructure designing approach among all these strategies, which can modulate the physicochemical properties in particular electronic structure of the active materials and promote the HER activity by the "so-called" synergistic effect.[14] In spite of these eye-catching progress, it is worth noting that the HER catalytic activity in alkaline solutions is usually two to three orders of magnitude lower than that in acids due to two distinct reaction routes in different solutions.[15] The most important reason is that hydrogen atoms directly come from H_3O^+ in acids, whereas they originate from water molecules for alkaline HER, which requires additional energy for accomplishing the water dissociation process.[16] In addition, many HER catalysts, especially their basal planes, including MoS_2, Co_2P are not favorable for water adsorption due to the lack of specific adsorption sites.[8a, 17] Moreover, hydroxyl ions (OH^-) in alkaline solutions also tend to adsorb on the catalyst surface, which is a competitive process as compared to water adsorption, and this will definitely slow down the overall HER kinetics.[18] Therefore, developing catalysts with good water adsorption/dissociation capability and high efficiency of adsorption and combination of H^* is vital to achieving competitive HER catalytic activity in alkaline solutions.

[a] G. Zhao, P. Li, Dr. K. Rui, Y. Chen, Prof. S. X. Dou, Dr. W. Sun
Institute for Superconducting and Electronic Materials, Australian Institute of Innovative Materials, University of Wollongong, Wollongong, NSW 2522, Australia
E-mail: wenping@uow.edu.au
Supporting information for this article is given via a link at the end of the document.

Recently, cubic-phase $CoSe_2$ (c-$CoSe_2$) was reported to deliver very appealing catalytic activity for HER in alkaline solution. And, it was found that, in addition to high electric conductivity and faster efficiency of converting H^* into H_2, the superior activity of c-$CoSe_2$ is closely associated with its competitive water adsorption capability.[19] In this work, we designed and synthesized $CoSe_2$/$MoSe_2$ heterostructures by decorating c-$CoSe_2$ quantum dots on $MoSe_2$ nanosheets towards enhanced alkaline HER catalytic performance. Benefiting from the unique water adsorption capability of c-$CoSe_2$, high efficiency of converting H^* into H_2 of $MoSe_2$, and the strong chemical bonding between the two compounds, the $CoSe_2$/$MoSe_2$ heterostructures exhibited substantially enhanced HER kinetics over $MoSe_2$ in alkaline media. In particular, the $CoSe_2$ quantum dots with a high density of edge sites provide sufficient active sites for water adsorption and dissociation, and hence continuously provide H^* for the subsequent hydrogen generation. To the best of our known, this is also the first TMD/TMD heterostructure reported for alkaline HER with exceptional catalytic performance. Our work provides an effective strategy for designing active catalysts for alkaline HER and is of great importance to the further development of hydrogen production by alkaline water electrolysis.

Results and Discussion

The synthesis of $CoSe_2$/$MoSe_2$ heterostructures involves a liquid-phase growth via a facile refluxing process and the following annealing in argon, as illustrated in Figure S1 (Supporting Information). Firstly, $Co(OH)_2$ was chemically deposited onto $MoSe_2$ nanosheets via the refluxing process at various atomic ratios of Co to Mo (Co:Mo=0.2, 0.5, and 1.0); taking Co:Mo=0.2 as an example, the formation of $0.2Co(OH)_2$/$MoSe_2$ can be evidenced by the X-ray diffraction (XRD) results (Figure S2a, Supporting Information). Then, the

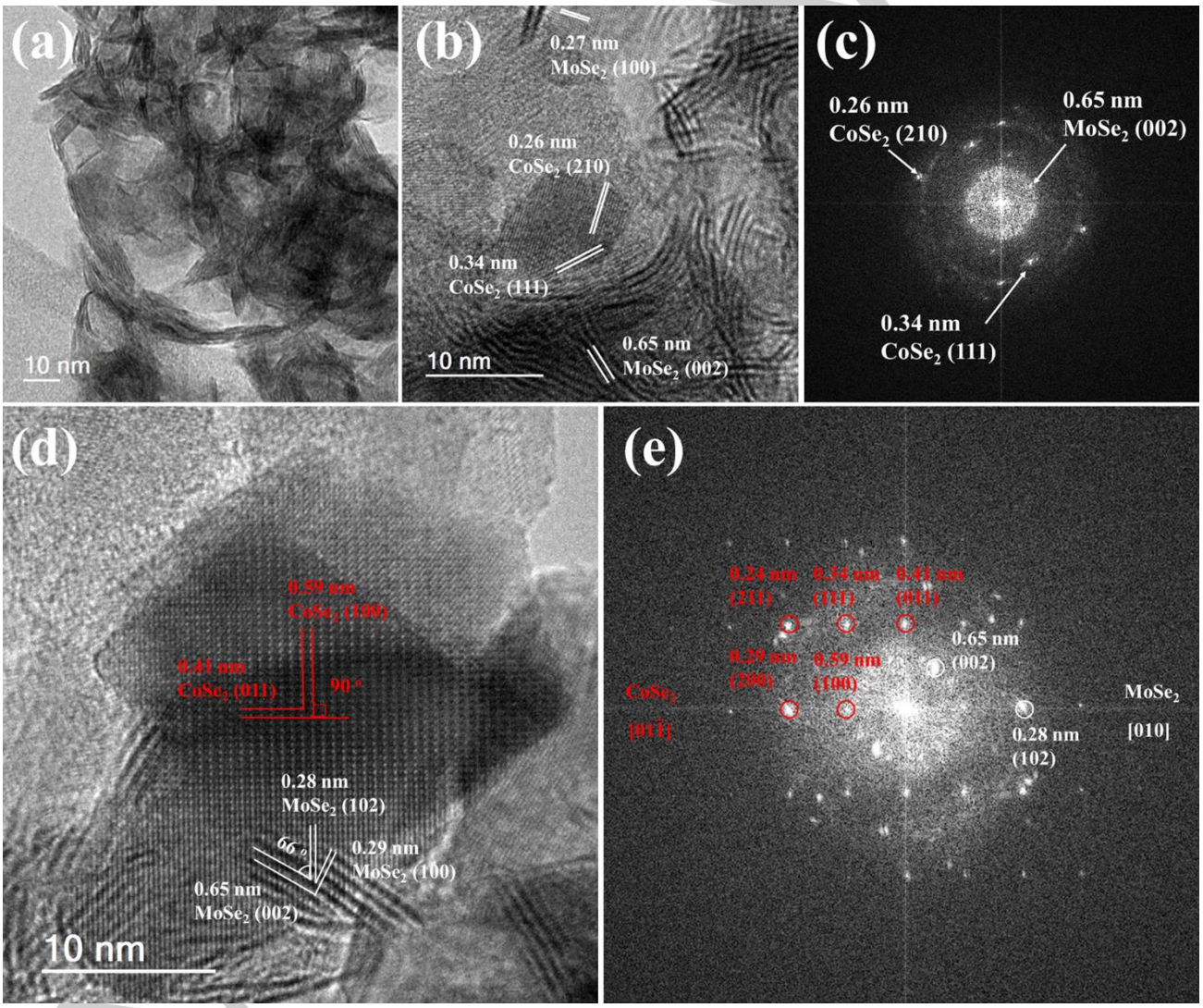

Figure 1. (a) TEM image of $0.2CoSe_2$/$MoSe_2$ heterostructure. (b) HRTEM image of $0.2CoSe_2$/$MoSe_2$ heterostructure. (c) The corresponding FFT pattern of (b). (d) HRTEM image of 0.5 $CoSe_2$/$MoSe_2$ heterostructure, showing the epitaxial structure. (e) The corresponding FFT pattern of (d).

$Co(OH)_2/MoSe_2$ composite was annealed at 300 °C for 2 h in argon, during which period $Co(OH)_2$ *in situ* converted into $CoSe_2$, resulting in the formation of $CoSe_2/MoSe_2$. The heterostructures are abbreviated as $0.2CoSe_2/MoSe_2$, $0.5CoSe_2/MoSe_2$, and $1.0CoSe_2/MoSe_2$ based on the Co/Mo ratio. Figure S2b (Supporting Information) showed the XRD patterns of the $CoSe_2/MoSe_2$ heterostructures. The diffraction peaks at 34.2 °, 46.5 °, and 51.7 ° can be assigned to the (210), (221), and (311) crystal planes of c-$CoSe_2$ (JCPDS # 89-2002), respectively,[20] while the peaks at 31.7 ° and 56.4 ° correspond to the (101) and (110) phases of hexagonal $MoSe_2$ (JCPDS # 72-1420), respectively.[21] To further verify the chemical reaction of $Co(OH)_2$ and $MoSe_2$, separately prepared $Co(OH)_2$ and $MoSe_2$ nanosheets were mixed homogeneously at an atom ratio of Co: Mo=0.2, and then were annealed under the same condition. In this case, orthorhombic $CoSe_2$ (o-$CoSe_2$, JCPDS 89-2003) is obtained rather than c-$CoSe_2$, as shown in Figure S2c (Supporting Information). Also, the as-prepared c-$CoSe_2$ is transform to o-$CoSe_2$ after being sintered at 300 °C in Ar for 2 h (Figure S2d, Supporting Information), indicating o-$CoSe_2$ is more thermodynamically stable at high temperature. Therefore, the formation of c-$CoSe_2$ after sintering the *in situ* grown $Co(OH)_2/MoSe_2$ heterostructures might be due to the confinement effect of the hexagonal $MoSe_2$ substrate.

Figure 1a shows the typical transmission electron microscopy (TEM) image of $0.2CoSe_2/MoSe_2$ heterostructures. The heterostructures keep the similar flexible and curved nanosheet morphology to that of $MoSe_2$ (Figure S3a, Supporting Information). C-$CoSe_2$ also possess nanosheets morphology as shown in Figure S3b (Supporting Information). The formation of $CoSe_2/MoSe_2$ heterostructure with $CoSe_2$ quantum dots anchored on $MoSe_2$ nanosheets can be well proved by the high-resolution TEM (HRTEM) image (Figure 1b) and the corresponding Fast Fourier Transformation (FFT) image (Figure 1c).[22] The lattice spacing of 0.26 and 0.34 nm can be assigned to the (210) and (111) crystal plane of c-$CoSe_2$, respectively, while the lattice spacing of 0.65 nm corresponds to the (002) crystal planes of $MoSe_2$. For the samples obtained by annealing the mixture of $Co(OH)_2$ and $MoSe_2$, similar morphology was achieved, and the lattice fringes corresponding to o-$CoSe_2$ and $MoSe_2$ can be indexed, as shown in Figure S3c-d (Supporting Information).

Interestingly, an epitaxial $CoSe_2/MoSe_2$ heterostructure is clearly revealed by the HRTEM image of $0.5CoSe_2/MoSe_2$, as shown in

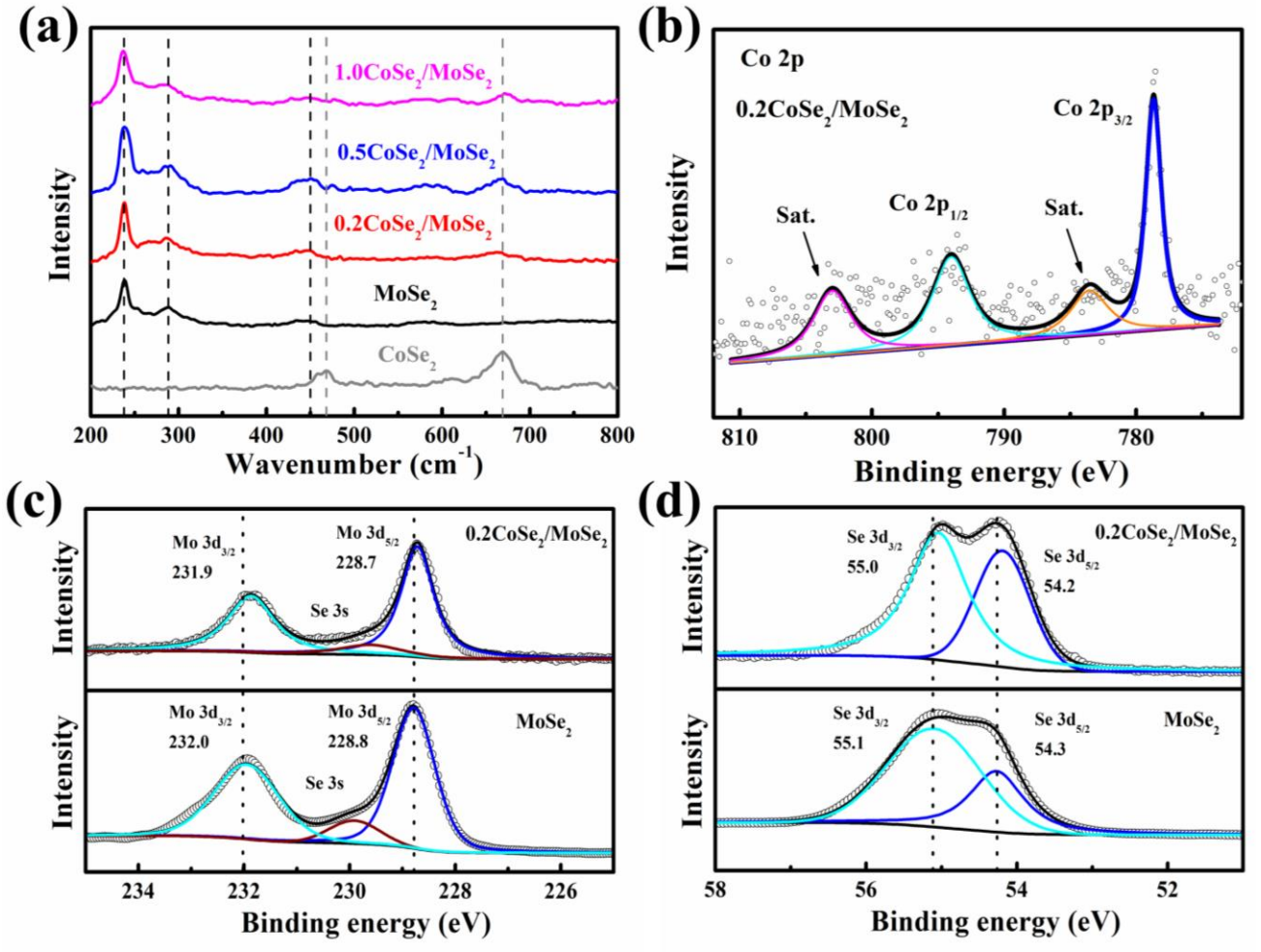

Figure 2. (a) Raman spectra of $MoSe_2$, $CoSe_2$, and $CoSe_2/MoSe_2$ heterostructures. High-resolution XPS spectra of 0.2 $CoSe_2/MoSe_2$ heterostructures: (b) Co 2p, (c) Mo 3d, and (d) Se 3d.

Figure 1c. The observed lattice fringes with a spacing of 0.41 nm and 0.59 nm can be attributed to the (011) and (100) crystal planes of c-$CoSe_2$, respectively. In the bottom part of Figure 1c, the lattice spacing of 0.65 nm and 0.29 nm can be assigned to the (002) and (100) planes of $MoSe_2$. The (102) planes of $MoSe_2$, 66 degrees to (002) planes, have a lattice spacing of 0.28 nm, which is approximately half the lattice spacing of (100) planes of c-$CoSe_2$. Therefore, it is reasonable to conclude that the epitaxial heterostructures of $CoSe_2$/$MoSe_2$ are present with the (100) plane of $CoSe_2$ in parallel with the (102) plane of $MoSe_2$. Figure 1e shows the FFT pattern of the epitaxial heterostructures, in which the cubic structure of $CoSe_2$ with a zone axis of [01$\bar{1}$] is evidently indexed. In addition, the pair of reciprocal dots at 0.29 nm could be assigned to the (200) planes of $CoSe_2$ and (102) planes of $MoSe_2$, confirming the epitaxial relation between $CoSe_2$ and $MoSe_2$. The zone axis of $MoSe_2$ is determined to be [010]. Based on the HRTEM and corresponding FFT analysis, the epitaxial relationship between $CoSe_2$ and $MoSe_2$ is defined as $(100)_{CoSe2}$ // $(102)_{MoSe2}$ or $[01\bar{1}]_{CoSe2}$ // $[010]_{MoSe2}$. To the best of our knowledge, this is the first observation of such epitaxial $CoSe_2$/$MoSe_2$ heterostructures. The Raman spectra of the $CoSe_2$/$MoSe_2$ heterostructures show the characteristic Raman bands of both $MoSe_2$ and $CoSe_2$, as shown in **Figure 2**a. The Raman bands at 237 cm^{-1}, 288 cm^{-1}, and 679 cm^{-1} can be assigned to the A_{1g} and $E_{2g}{}^1$ modes of $MoSe_2$ and the A_{1g} mode of $CoSe_2$, respectively;[23] while the broad band at 450 and 457 cm^{-1} may originate from the A_g mode of molybdenum oxide and E_g mode of cobalt oxide, respectively, which can be ascribed to the surface oxidation during Raman test.[24] The chemical composition and elemental states of the $CoSe_2$/$MoSe_2$ heterostructures were further characterized by X-ray photoelectron spectroscopy (XPS), as presented in Figure 2b-d. Taking 0.2$CoSe_2$/$MoSe_2$ as an example, the peaks at 778.8 and 793.9 eV in Figure 2b can be assigned to Co $2p_{3/2}$ and Co $2p_{1/2}$, and the satellite peaks of Co $2p_{3/2}$ and Co $2p_{1/2}$ are located at 786.5 and 803.0 eV, indicating the presence of Co^{2+} in $CoSe_2$.[25] Figure 2c-d show the high-resolution XPS spectra of Mo 3d and Se 3d. The binding energies of Mo 3d and Se 3d of 0.2$CoSe_2$/$MoSe_2$ are almost consistent with those of $MoSe_2$, indicating no apparent electronic interaction between $MoSe_2$ and $CoSe_2$.

The HER performance of $CoSe_2$/$MoSe_2$ heterostructures together with bare $MoSe_2$ and $CoSe_2$ were assessed in N_2-saturated 1 M KOH using a conventional three-electrode cell.

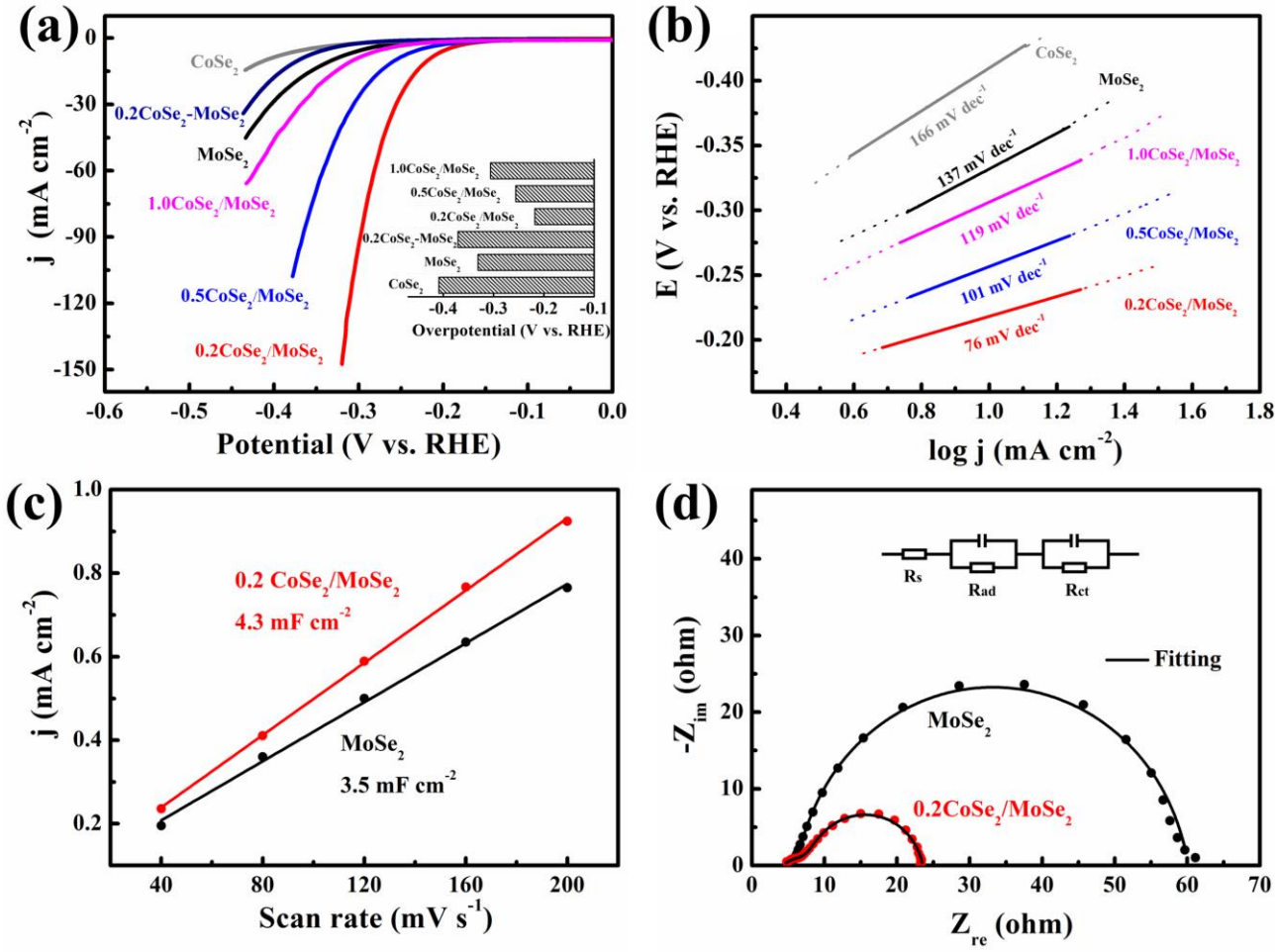

Figure 3. (a) LSV curves of $MoSe_2$, $CoSe_2$, and $CoSe_2$/$MoSe_2$ heterostructures. (b) The corresponding Tafel plots of the LSV curves. (c) The fitted C_{dl} of $MoSe_2$ and 0.2$CoSe_2$/$MoSe_2$ heterostructure. (d) EIS of 0.2 $CoSe_2$/$MoSe_2$ heterostructure, and the inset is the equivalent circuit used for fitting.

The catalysts were coated on the glassy carbon (GC) electrode for linear sweep voltammetry (LSV) testing, and all the presented LSV data were corrected with 95% iR compensation, as shown in **Figure 3**a. Due to the sluggish water dissociation step, the $MoSe_2$ and $CoSe_2$ nanosheets exhibited inferior catalytic activity in 1 M KOH as compared with that in 0.5 M H_2SO_4 (Figure S4, Supporting Information), which is in consistence with previous reports.[10a] An overpotential of 331 mV is required to reach a current density of 10 mA cm^{-2} for $MoSe_2$ nanosheets, while $CoSe_2$ nanosheets showed even worse activity, requiring an overpotential of 409 mV. The alkaline HER activity is substantially enhanced by incorporating $CoSe_2$ quantum dots on $MoSe_2$ nanosheets. $0.2CoSe_2/MoSe_2$ turns out to be the optimal composition, and it only requires an overpotential of as low as 218 mV to obtain a cathodic current density of 10 $mAcm^{-2}$. Further increasing the amount of less active $CoSe_2$, the overpotentials of $0.5CoSe_2/MoSe_2$ and $1.0CoSe_2/MoSe_2$ increase accordingly, but their activity still exceeds bare $MoSe_2$ and $CoSe_2$. It has to be noted that the performance of $0.2CoSe_2/MoSe_2$ is one of the best among conductive support-free and precious metal-free catalysts for alkaline HER, and even comparable to the acid HER performance of similar materials (Table S1, Supporting Information). Meanwhile, a control sample by physically mixing $CoSe_2$ and $MoSe_2$ at similar Co/Mo atom ratio ($0.2CoSe_2$-$MoSe_2$) was also evaluated for comparison, but its activity (371 mV at 10 mA cm^{-2}) is much inferior to that of $0.2CoSe_2/MoSe_2$ and even $MoSe_2$. This result indicating that the performance improvement of the heterostructures is more likely associated with the well-defined nanostructures, particularly monodispersed $CoSe_2$ quantum dots with abundant edge sites and the chemical bonding between the two components. Further, the performance durability of the $CoSe_2/MoSe_2$ heterostructures was evaluated via an accelerated degradation test.[26] As shown in Figure S5 (Supporting Information), the catalyst shows an overpotential increase of merely 15 mV at a current density of 10 mA cm^{-2} after the degradation test. In addition, TEM and HRTEM images show a well-preserved morphology as well as clear lattice fringes of both $MoSe_2$ and $CoSe_2$ after the degradation test (Figure S6a-b, Supporting Information), demonstrating good durability of the $CoSe_2/MoSe_2$ heterostructures.

The HER kinetics was further analyzed based on the corresponding Tafel plots as shown in Figure 3b. The Tafel slope was calculated to be 137 and 166 mV dec^{-1} for bare $MoSe_2$ and $CoSe_2$, respectively. Such large Tafel slop values indicate that water dissociation (Volmer reaction) is the rate determining step (RDS) of HER on these catalyst surfaces in alkaline solution.[27] By contrast, the $CoSe_2/MoSe_2$ heterostructures show greatly decreased Tafel slops, and particularly the Tafel slope is reduced to as low as 76 mV dec^{-1} for $0.2CoSe_2/MoSe_2$, suggesting the HER kinetics is determined by the Volmer reaction and the following Heyrovsky reaction.[28] The enhanced HER activity is probably induced by the accelerated water dissociation process. This theory could be supported by the fact that, the HER activity of $CoSe_2/MoSe_2$ is not enhanced compared with $MoSe_2$ and $CoSe_2$ in 0.5 M H_2SO_4, as shown in Figure S4a. The small Tafel slopes in acidic media demonstrate the fast hydrogen adsorption process on both $MoSe_2$ and $CoSe_2$ surfaces (Figure S7, Supporting Information).[28] Also, it was reported that the adsorption behavior of hydrogen on the catalyst surfaces is pH-independent.[13a, 29] In other words, similar hydrogen adsorption behavior should also occur on $MoSe_2$ and $CoSe_2$ surfaces in alkaline media. Therefore, it can be concluded that the enhanced alkaline HER performance of $CoSe_2/MoSe_2$ heterostructures is ascribed to the accelerated water adsorption and dissociation process on $CeSe_2$.

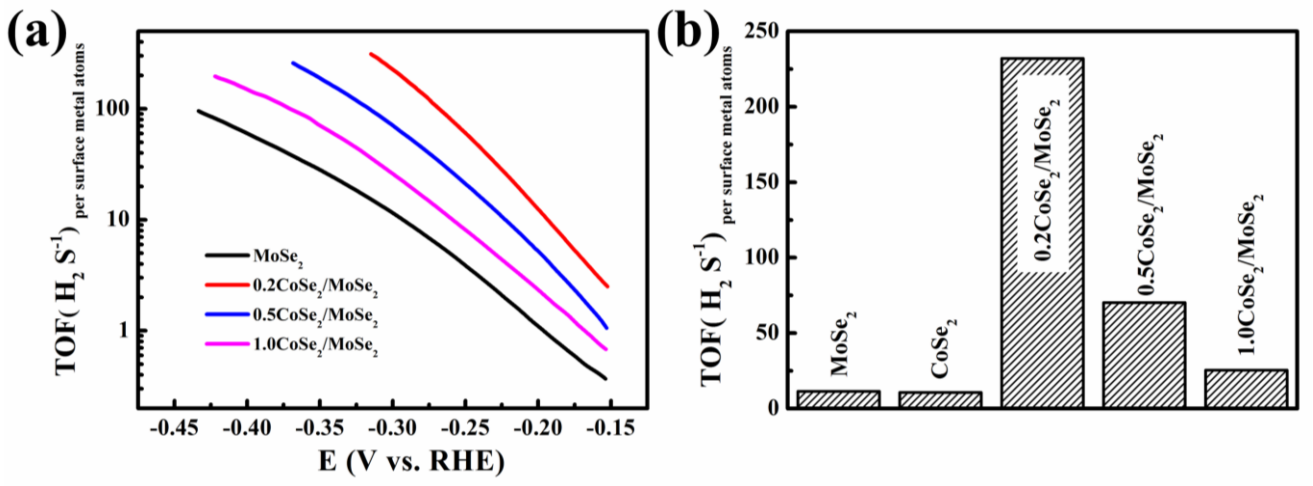

Figure 4. (a) TOF per surface Mo atom of $MoSe_2$ and $CoSe_2/MoSe_2$ heterostructures. (b) TOF per surface Mo atom at an overpotential of 300 mV.

In order to gain deeper insights into understanding the accelerated reaction kinetics, the electrochemical active specific area (ECSA) of the catalysts was evaluated based on the double layer capacitance (C_{dl}), which were determined from the cyclic voltammetry (CV) results acquired at various scan rates (Figure S8a-b, Supporting Information). As shown in Figure 3c, the fitted C_{dl} of 0.2$CoSe_2$/$MoSe_2$ is 4.3 mF cm^{-2}, which is close to that of bare $MoSe_2$ (3.5 mF cm^{-2}). Such result reveals that the promoted HER performance should be derived from the enhanced intrinsic activity rather than the increased ECSA or active sites. The electrochemical impedance spectra (EIS) were measured at the potential of -300 mV vs. RHE (Figure 3d). The Nyquist plot could be fitted with an equivalent circuit consisting of an evident semicircle at low-frequency region that represents the charge transfer and mass diffusion process and a less obvious semicircle at high-frequency region which corresponds to the pseudocapacitance of the adsorbed species.[30] The fitted results suggest almost the same adsorption resistance and capacitance of 0.2$CoSe_2$/$MoSe_2$ and $MoSe_2$, which is in accordance with the ECSA result. But, 0.2$CoSe_2$/$MoSe_2$ shows dramatically reduced low-frequency resistance, confirming the largely accelerated catalytic reaction kinetics.

To evaluate the intrinsic HER activity of these catalysts, the turnover frequency (TOF) was calculated based on the number of surface metal atoms. The TOF values at different overpotentials were calculated as shown in **Figure 4**a. The $CoSe_2$/$MoSe_2$ heterostructures exhibit much larger TOF than $MoSe_2$ and $CoSe_2$ nanosheets. In particular, the TOF of 0.2$CoSe_2$/$MoSe_2$ is 232 s^{-1} at an overpotential of 300 mV, more than 20 time as high as that of $MoSe_2$ and $CoSe_2$ nanosheets (11.4 s^{-1} for $MoSe_2$ and 10.7 for $CoSe_2$, Figure 4b). This dramatically increased TOF confirms the substantial increment of the intrinsic activity. As has been mentioned earlier, the enhanced HER activity for the $CoSe_2$/$MoSe_2$ heterostructures is likely to originate from the accelerated water adsorption and dissociation process on $CeSe_2$. In addition, Chen et al. reported that c-$CoSe_2$ delivered much higher catalytic activity than o-$CoSe_2$ for alkaline HER, and they found that the superior water adsorption capability of c-$CoSe_2$ is vital to the enhanced activity.[19] On the basis of Chen's report, it can be speculated that the accelerated water adsorption/dissociation induced by the well-defined c-$CoSe_2$ quantum dots is responsible for the substantially enhanced alkaline HER catalytic activity of 0.2$CoSe_2$/$MoSe_2$. As illustrated in **Figure 5**, the $CoSe_2$ species can provide enough water adsorption sites, and hence the water dissociation process, as well as the following Heyrovsky reaction, could be accelerated; meanwhile, the continuously generated H* will diffuse and adsorb on $MoSe_2$ surface, and then be transformed into H_2. This synergetic effect between $CoSe_2$ and $MoSe_2$ ensures the enhanced HER activity of the $CoSe_2$/$MoSe_2$ heterostructures in alkaline media.

The importance of the *in situ* formed water adsorption/dissociation sites in this synergetic effect could be further highlighted by comparing the HER performance of 0.2 $CoSe_2$/$MoSe_2$ and the 0.2o-$CoSe_2$/$MoSe_2$ heterostructures. As shown in Figure S9 (Supporting Information), 0.2o-$CoSe_2$/$MoSe_2$ heterostructures also deliver enhanced alkaline HER catalytic activity over $MoSe_2$ with lower overpotential and smaller Tafel slope, however, the performance improvement of 0.2o-$CoSe_2$/$MoSe_2$ is not so significantly as 0.2$CoSe_2$/$MoSe_2$ due to the inferior water adsorption capability of o-$CeSe_2$. The water adsorption energy for o-$CoSe_2$ and c-$CoSe_2$ was calculated to be -0.106 and -0.163 eV, respectively.[19] On this basis, c-$CoSe_2$ provides a more easily formed catalyst-water state, and then the water dissociation process could be subsequently accelerated more significantly. Consequently, 0.2$CoSe_2$/$MoSe_2$ heterostructures with c-$CoSe_2$ will have a faster HER process than 0.2o-$CoSe_2$/$MoSe_2$. These results together with Chen's report further confirm that the in situ formed c-$CoSe_2$ quantum dots can accelerate the water adsorption/dissociation process and hence grant the substantially enhanced alkaline HER catalytic activity of 0.2$CoSe_2$/$MoSe_2$.

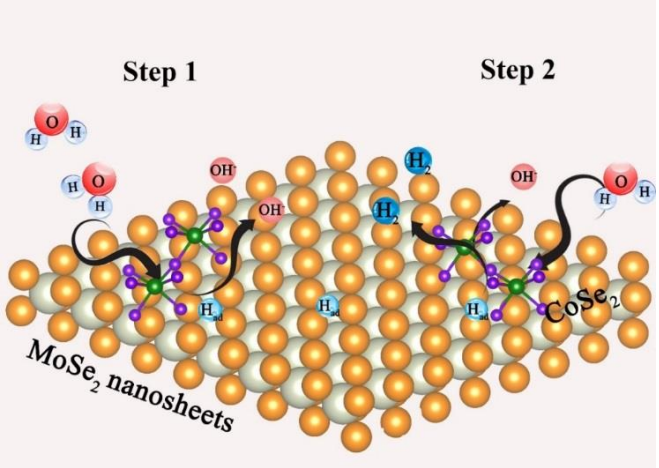

Figure 5. Illustration of the HER mechanism on $CoSe_2$/$MoSe_2$ heterostructures in alkaline media, showing the synergetic effect between $CoSe_2$ and $MoSe_2$

Conclusions

In summary, we designed and synthesized $CoSe_2$/$MoSe_2$ heterostructures with water-adsorption-favored $CoSe_2$ species decorated on $MoSe_2$ nanosheets via a facile refluxing process followed by annealing in argon. An epitaxial $CoSe_2$/$MoSe_2$ structure defined as $(100)_{CoSe2}$ // $(102)_{MoSe2}$ or $[01\bar{1}]_{CoSe2}$ // $[010]_{MoSe2}$ was observed for the first time. The $CoSe_2$/$MoSe_2$ heterostructures exhibited largely substantially enhanced HER catalytic activity in 1 M KOH as compared with $MoSe_2$ and $CoSe_2$. In particular, 0.2$CoSe_2$/$MoSe_2$ showed the best performance with a low overpotential of 220 mV at 10 mA cm^{-2} and a small Tafel slope of 76 mV dec^{-1}. TOF analysis shows the 0.2$CoSe_2$/$MoSe_2$ heterostructures possesses superior intrinsic activity to many state-of-the-art catalysts. Further, the detailed electrochemical analysis suggests that the improved alkaline HER catalytic activity originates from the synergetic effect between $CoSe_2$ and $MoSe_2$, where the water adsorption/dissociation process can be accelerated by the additional water adsorption sites provided by $CoSe_2$ species and the following processes can rapidly take place on the

abundant exposed $MoSe_2$ species. The present results provide new ideas for designing and synthesizing functional heterostructures for efficient alkaline HER and other related energy applications.

Experimental Section

All chemicals were purchased from Sigma-Aldrich (A.R) and were used as received without further purification. Ultrapure deionized water (DI-water; 18 MΩ/cm) was used in all experiments.

Preparation of $MoSe_2$ and $CoSe_2$ nanosheets. $MoSe_2$ nanosheets were prepared via a hydrothermal method followed by annealing in an argon atmosphere. In a typical synthesis procedure, 0.2g $NaBH_4$, 1 mmol Na_2MoO_4, and 2 mmol Se powder were dissolved in 35 mL DI-water under continuous stirring. The obtained suspensions were then transferred to a 50 mL Teflon-lined stainless steel autoclave. After that, the autoclave was sealed and kept at 180 °C for 24 h in oven and then cooled down to room temperature naturally. The precipitates were collected by centrifugation and washed with ethanol and DI-water several times. After drying at 60 °C in vacuum overnight and subsequent annealing at 300 °C in an argon atmosphere, $MoSe_2$ nanosheets were obtained. Cubic $CoSe_2$ nanosheets were prepared via the same procedure except that 1 mmol $Co(NO_3)_2{\cdot}6H_2O$ were added instead of Na_2MoO_4. Orthorhombic $CoSe_2$ was obtained by sintering cubic $CoSe_2$ nanosheets at 300 °C in an argon atmosphere for 2 h.

Preparation of $CoSe_2$/$MoSe_2$ heterostructures. Typically, 64 mg $MoSe_2$ nanosheets were dispersed in EtOH and treated with ultrasonication for 3 h. The stoichiometric amounts of $Co(NO_3)_2{\cdot}6H_2O$ and urea (CH_4N_2O) were dissolved in the suspension under magnetic stirring together with 5 mL DI-water and 20 mL ethylene glycol (EG). The suspensions were then transferred to a three neck flask, followed by heating at 96 °C for 2 h under reflux conditions with continuous magnetic stirring and argon protection. After cooling down to room temperature, the precipitates were collected by centrifugation, washed with EtOH and DI-water several times, and dried at 60 °C in vacuum overnight. Eventually, the $CoSe_2$/$MoSe_2$ heterostructures were obtained by further sintering at 300 °C in an argon atmosphere for 2 h.

Preparation of 0.2o-$CoSe_2$/$MoSe_2$ heterostructures. $Co(OH)_2$ was prepared via the same refluxing procedure as $CoSe_2$/$MoSe_2$ heterostructures except that no $MoSe_2$ nanosheet suspensions were added. Then the separately prepared $Co(OH)_2$ and $MoSe_2$ nanosheets were thoroughly mixed with a Co/Mo atomic ratio of 0.2. The mixture was then sintered at 300 °C in argon for 2 h.

Materials Characterization. XRD patterns were recorded on a GBC enhanced mini-materials analyser (GBC eMMA) X-Ray diffractometer with a Cu Kα radiation (λ=1.541 Å, 25 mA, 40 kV, 1 ° min^{-1} from 10 ° to 60 °). Raman spectra were obtained using a Raman JY HR800 Spectrometer with a 632.8 nm Helium-Neon gas laser with spatial resolution down to 1 um and spectral resolution down to 0.35 cm^{-1}. The surface chemical state was detected by X-ray photoelectron spectroscopy (XPS, Phoibos 100 Analyser, SPECS, Germany, Al K_α X-rays). TEM and HRTEM images were taken with a JEOL 2010 microscope at the accelerating voltage of 200 kV.

Electrochemical test. Electrochemical tests in alkaline solution were conducted with a rotate disc electrode (RDE) system in 1 M KOH aqueous solution using a standard three-electrode electrochemical cell with Pt foil and Hg/HgO (1 M KOH) as the counter and the reference electrode, respectively. An Ag/AgCl electrode was used as the reference electrode in acid solution (0.5 M H_2SO_4). For the preparation of working electrodes, 4 mg of catalysts were dispersed in 32 μL 5 wt% Nafion solution, 768 uL DI-water and 200 uL isopropanol by 3 h ultrasonication to form a homogeneous ink. Then 10 μL of the catalyst ink (containing 40 μg of catalyst) was loaded onto a glassy carbon electrode of 5 mm in diameter (loading ~ 0.204 mg cm^{-2}) and dried naturally in the ambient air.

Electrochemical experiments were operated on a BioLogic VSP 300 electrochemical workstation. Prior to HER tests, the test solution was bubbled with high-purity nitrogen for at least 30 min to remove any dissolved oxygen. During the measurements, the working electrode was constantly rotated at 1600 rpm to alleviate the effect of diffusion. All potentials reported are referenced to the reversible hydrogen electrode (RHE), and the ohmic potential drop caused by the solution resistance has been corrected with 95% iR-compensation. Linear sweep voltammetry (LSV) was performed at 5 mV s^{-1} from 0 V to -0.5 V vs. RHE. The accelerated degradation test was performed by sweeping the potential in a range of -400 mV ~ 0 mV vs. RHE at a sweep rate of 100 mV s^{-1}. Electrochemical impedance spectra (EIS) was measured at various potentials in the frequency range of 100 kHz~100 mHz at the amplitude of the sinusoidal voltage of 10 mV, and the results were fitted with ZSimpWin software.

Calculation of the double-layer capacitance. The materials electrochemically active surface area (ECSA) is evaluated by calculating the double-layer capacitance (C_{dl}) of the electrodes in 1 M KOH. Cyclic voltammetry (CV) at 40, 80, 120, 160 and 200 mV s^{-1} were performed to evaluate the capacitive behaviour of the electrodes, then C_{dl} was calculated according to equation 1.

$$C_{dl} = \frac{0.5(|j_a| + |j_c|)}{\nu} \qquad \text{equation 1}$$

j_a—anodic current density, mA cm^{-2}

j_c—cathodic current density, mA cm^{-2}

ν—scan rate, mV s^{-1}

Calculation of the turnover frequency. The turnover frequency (TOF) is calculated based on the definition of TOF (equation 2). First, the as-measured current density was normalized by subtracting the capacitive current density to get the HER current density. Then the total number of H_2 molecules generated per second was obtained using Faraday's law of electrolysis (equation 3). The surface metal atom density was introduced to evaluate the number of active sites, which was estimated to be 1.46×10^{15} cm^{-2} and 4.17×10^{14} cm^{-2} for $MoSe_2$ and $CoSe_2$ based on their lattice constants, respectively.

$$TOF = \frac{\text{Generated } H_2 \text{ molecule number per second}}{\text{Number of active sites}}$$ equation 2

$$H_2 \text{ molecule number} = \frac{Q}{2F} \cdot N_A = \frac{j \cdot t}{1000} \cdot \frac{1}{2F} \cdot N_A$$ equation 3

Q—quantity of electric charge, C
F—Faraday's constant, 96485 c/mol
N_A—Avogadro constant, 6.02×10^{23}
j—HER current density, mA cm^{-2}
t—unit time, 1s

Acknowledgements

This work was financially supported by the Australian Research Council (ARC) DECRA Grant (DE160100596) and AIIM FOR GOLD Grant (2017, 2018). The authors acknowledge use of facilities within the UOW electron Microscopy Center.

Keywords: hydrogen evolution reaction • heterostructures • alkaline media • synergetic effect • transition metal dichalcogenides

[1] L. Schlapbach, A. Züttel, *Nature* **2001**, *414*, 353.
[2] a) M. G. Walter, E. L. Warren, J. R. McKone, S. W. Boettcher, Q. Mi, E. A. Santori, N. S. Lewis, *Chem.Rev.* **2010**, *110*, 6446-6473; b) T. Liu, L. Xie, J. Yang, R. Kong, G. Du, A. M. Asiri, X. Sun, L. Chen, *ChemElectroChem* **2017**, *4*, 1840-1845; c) K. Rui, G. Zhao, Y. Chen, Y. Lin, Q. Zhou, J. Chen, J. Zhu, W. Sun, W. Huang, S. X. Dou, *Adv. Funct. Mater.* **2018**, 1801554.
[3] a) S. T. Hunt, M. Milina, A. C. Alba-Rubio, C. H. Hendon, J. A. Dumesic, Y. Román-Leshkov, *Science* **2016**, *352*, 974-978; b) H.-S. Oh, H. N. Nong, T. Reier, M. Gliech, P. Strasser, *Chem. Sci.* **2015**, *6*, 3321-3328; c) X. Ji, B. Liu, X. Ren, X. Shi, A. M. Asiri, X. Sun, *ACS Sustainable Chemistry & Engineering* **2018**, *6*, 4499-4503.
[4] G. F. Chen, T. Y. Ma, Z. Q. Liu, N. Li, Y. Z. Su, K. Davey, S. Z. Qiao, *Adv. Funct. Mater.* **2016**, *26*, 3314-3323.
[5] a) Y. Zhang, Q. Zhou, J. Zhu, Q. Yan, S. X. Dou, W. Sun, *Adv. Funct. Mater.* **2017**, *27*; b) C. Tang, N. Cheng, Z. Pu, W. Xing, X. Sun, *Angew. Chem.* **2015**, *127*, 9483-9487.
[6] a) Y. Shi, B. Zhang, *Chem. Soc. Rev.* **2016**, *45*, 1529-1541; b) Y. Zhong, X. Xia, F. Shi, J. Zhan, J. Tu, H. J. Fan, *Adv. Sci.* **2016**, *3*; c) C. Tang, R. Zhang, W. Lu, L. He, X. Jiang, A. M. Asiri, X. Sun, *Adv. Mater.* **2017**, *29*.
[7] P. Jiang, Q. Liu, X. Sun, *Nanoscale* **2014**, *6*, 13440-13445.
[8] a) K. Xu, H. Ding, M. Zhang, M. Chen, Z. Hao, L. Zhang, C. Wu, Y. Xie, *Adv. Mater.* **2017**, *29*; b) Q. Liu, L. Xie, F. Qu, Z. Liu, G. Du, A. M. Asiri, X. Sun, *Inorganic Chemistry Frontiers* **2017**, *4*, 1120-1124.
[9] a) B. Hinnemann, P. G. Moses, J. Bonde, K. P. Jørgensen, J. H. Nielsen, S. Horch, I. Chorkendorff, J. K. Nørskov, *J. Am. Chem. Soc.* **2005**, *127*, 5308-5309; b) M. A. Lukowski, A. S. Daniel, F. Meng, A. Forticaux, L. Li, S. Jin, *J. Am. Chem. Soc.* **2013**, *135*, 10274-10277; c) L. Tao, X. Duan, C. Wang, X. Duan, S. Wang, *Chem. Commun.* **2015**, *51*, 7470-7473.
[10] a) J. D. Wiensch, J. John, J. M. Velazquez, D. A. Torelli, A. P. Pieterick, M. T. McDowell, K. Sun, X. Zhao, B. S. Brunschwig, N. S. Lewis, *ACS Energy Lett.* **2017**, *2*, 2234-2238; b) Y. Yin, Y. Zhang, T. Gao, T. Yao, X. Zhang, J. Han, X. Wang, Z. Zhang, P. Xu, P. Zhang, *Adv. Mater.* **2017**, *29*.
[11] a) Y. Sun, F. Alimohammadi, D. Zhang, G. Guo, *Nano Lett.* **2017**, *17*, 1963-1969; b) J. X. Feng, L. X. Ding, S. H. Ye, X. J. He, H. Xu, Y. X. Tong, G. R. Li, *Adv. Mater.* **2015**, *27*, 7051-7057.
[12] a) J. Zhang, T. Wang, P. Liu, S. Liu, R. Dong, X. Zhuang, M. Chen, X. Feng, *Energy Environ. Sci.* **2016**, *9*, 2789-2793; b) C. Ouyang, X. Wang, S. Wang, *Chem. Commun.* **2015**, *51*, 14160-14163.
[13] a) Z. W. Seh, J. Kibsgaard, C. F. Dickens, I. Chorkendorff, J. K. Nørskov, T. F. Jaramillo, *Science* **2017**, *355*, eaad4998; b) H. Li, C. Tsai, A. L. Koh, L. Cai, A. W. Contryman, A. H. Fragapane, J. Zhao, H. S. Han, H. C. Manoharan, F. Abild-Pedersen, *Nat. Mater.* **2016**, *15*, 48.
[14] a) Y. Chen, Q. Zhou, G. Zhao, Z. Yu, X. Wang, S. X. Dou, W. Sun, *Adv. Funct. Mater.* **2018**, *28*; b) J. X. Feng, H. Xu, Y. T. Dong, X. F. Lu, Y. X. Tong, G. R. Li, *Angew. Chem.* **2017**, *129*, 3006-3010.
[15] a) J. Staszak-Jirkovský, C. D. Malliakas, P. P. Lopes, N. Danilovic, S. S. Kota, K.-C. Chang, B. Genorio, D. Strmcnik, V. R. Stamenkovic, M. G. Kanatzidis, *Nat. Mater.* **2016**, *15*, 197; b) W. Sheng, H. A. Gasteiger, Y. Shao-Horn, *J. Electrochem. Soc.* **2010**, *157*, B1529-B1536.
[16] a) J. Durst, C. Simon, A. Siebel, P. J. Rheinländer, T. Schuler, M. Hanzlik, J. Herranz, F. Hasché, H. A. Gasteiger, *ECS Trans.* **2014**, *64*, 1069-1080; b) L. Xie, X. Ren, Q. Liu, G. Cui, R. Ge, A. M. Asiri, X. Sun, Q. Zhang, L. Chen, *J. Mater. Chem. A* **2018**.
[17] K. K. Ghuman, S. Yadav, C. V. Singh, *The Journal of Physical Chemistry C* **2015**, *119*, 6518-6529.
[18] a) M. Gong, W. Zhou, M.-C. Tsai, J. Zhou, M. Guan, M.-C. Lin, B. Zhang, Y. Hu, D.-Y. Wang, J. Yang, *Nat. Commun* **2014**, *5*, 4695; b) D. Strmcnik, P. P. Lopes, B. Genorio, V. R. Stamenkovic, N. M. Markovic, *Nano Energy* **2016**, *29*, 29-36.
[19] P. Chen, K. Xu, S. Tao, T. Zhou, Y. Tong, H. Ding, L. Zhang, W. Chu, C. Wu, Y. Xie, *Advanced Materials* **2016**, *28*, 7527-7532.
[20] P. Ramdohr, M. Schmitt, *Neues Jahrb Mineral Monatsh* **1955**, *6*, 133-142.
[21] L. C. Towle, V. Oberbeck, B. E. Brown, R. E. Stajdohar, *Science* **1966**, *154*, 895-896.
[22] W. Maneeprakorn, M. A. Malik, P. O'Brien, *J. Mater. Chem.* **2010**, *20*, 2329-2335.
[23] a) S. V. Bhatt, M. Deshpande, V. Sathe, R. Rao, S. Chaki, *J. Raman Spectrosc.* **2014**, *45*, 971-979; b) P. Tonndorf, R. Schmidt, P. Böttger, X. Zhang, J. Börner, A. Liebig, M. Albrecht, C. Kloc, O. Gordan, D. R. Zahn, *Opt. Express* **2013**, *21*, 4908-4916.
[24] a) D. Nam, J. U. Lee, H. Cheong, *Sci Rep* **2015**, *5*, 17113; b) R. K. Sharma, G. Reddy, *J. Phys. D: Appl. Phys.* **2014**, *47*, 065305.
[25] a) S.-K. Park, J. K. Kim, Y. C. Kang, *Chem. Eng. J.* **2017**, *328*, 546-555; b) Y. Tang, Z. Zhao, X. Hao, Y. Wang, Y. Liu, Y. Hou, Q. Yang, X. Wang, J. Qiu, *J. Mater. Chem. A* **2017**, *5*, 13591-13600; c) C. Strydom, H. Strydom, *Inorg. Chim. Acta* **1989**, *159*, 191-195.
[26] X. Wang, Y. V. Kolen'ko, X. Q. Bao, K. Kovnir, L. Liu, *Angew. Chem., Int. Ed.* **2015**, *54*, 8188-8192.
[27] B. Tilak, C.-P. Chen, *J. Appl. Electrochem.* **1993**, *23*, 631-640.
[28] Y. Li, H. Wang, L. Xie, Y. Liang, G. Hong, H. Dai, *J. Am. Chem. Soc.* **2011**, *133*, 7296-7299.
[29] T. Schmidt, P. Ross Jr, N. Markovic, *J. Electroanal. Chem.* **2002**, *524*, 252-260.
[30] D. Harrington, B. Conway, *Electrochim. Acta* **1987**, *32*, 1703-1712.

10.1002/chem.201801693

WILEY-VCH

Entry for the Table of Contents

FULL PAPER

Highly active TMD-based heterostructures towards alkaline hydrogen evolution reaction (HER) are designed and synthesized by constructing water adsorption sites on $MoSe_2$ nanosheets surface. Our results provide an effective strategy for developing earth-abundant catalysts with high activity for alkaline HER and are of great significance to promote the practical application of alkaline

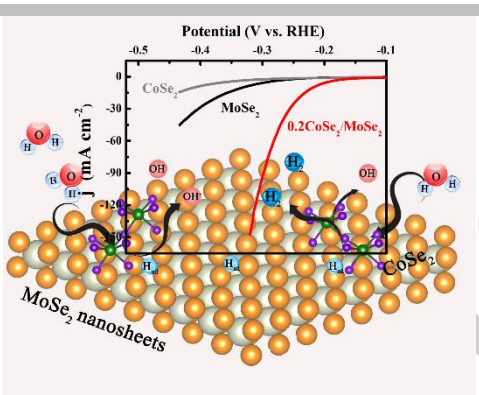

Guoqiang Zhao,[a] Peng Li,[a] Kun Rui,[a] Yaping Chen,[a] Shi Xue Dou,[a] Wenping Sun[a,*]

Page No. – Page No.

$CoSe_2/MoSe_2$ Heterostructures with Enriched Water Adsorption/Dissociation Sites towards Enhanced Alkaline Hydrogen Evolution Reaction